ACS NANO

www.acsnano.org

ARTICLE

Wafer-Scale Epitaxial Growth of Unidirectional WS_2 Monolayers on Sapphire

Mikhail Chubarov,[#] Tanushree H. Choudhury,[*,#] Danielle Reifsnyder Hickey, Saiphaneendra Bachu, Tianyi Zhang, Amritanand Sebastian, Anushka Bansal, Haoyue Zhu, Nicholas Trainor, Saptarshi Das, Mauricio Terrones, Nasim Alem, and Joan M. Redwing*

Cite This: *ACS Nano* 2021, 15, 2532−2541

Read Online

ACCESS | Metrics & More | Article Recommendations | Supporting Information

ABSTRACT: **Realization of wafer-scale single-crystal films of transition metal dichalcogenides (TMDs) such as WS_2 requires epitaxial growth and coalescence of oriented domains to form a continuous monolayer. The domains must be oriented in the same crystallographic direction on the substrate to inhibit the formation of inversion domain boundaries (IDBs), which are a common feature of layered chalcogenides. Here we demonstrate fully coalesced unidirectional WS_2 monolayers on 2 in. diameter *c*-plane sapphire by metalorganic chemical vapor deposition using a multistep growth process to achieve epitaxial WS_2 monolayers with low in-plane rotational twist (0.09°).**

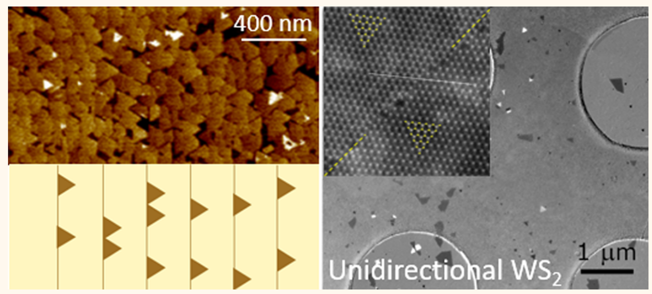

Transmission electron microscopy analysis reveals that the WS_2 monolayers are largely free of IDBs but instead have translational boundaries that arise when WS_2 domains with slightly offset lattices merge together. By regulating the monolayer growth rate, the density of translational boundaries and bilayer coverage were significantly reduced. The unidirectional orientation of domains is attributed to the presence of steps on the sapphire surface coupled with growth conditions that promote surface diffusion, lateral domain growth, and coalescence while preserving the aligned domain structure. The transferred WS_2 monolayers show neutral and charged exciton emission at 80 K with negligible defect-related luminescence. Back-gated WS_2 field effect transistors exhibited an $I_{ON}/_{OFF}$ of $\sim10^7$ and mobility of 16 $cm^2/(V\ s)$. The results demonstrate the potential of achieving wafer-scale TMD monolayers free of inversion domains with properties approaching those of exfoliated flakes.

KEYWORDS: *wafer-scale, epitaxy, unidirectional, transition metal dichalcogenide, WS_2, monolayer, MOCVD*

Tungsten disulfide (WS_2), in the monolayer limit, exhibits a direct bandgap with near bandgap emission at 2 eV,[1] has a relatively high mobility,[2] and exhibits valley polarization.[3] WS_2 monolayers and heterostructures are therefore of interest for fundamental studies and device applications such as photodetectors[4] and field effect transistors.[2] To achieve commercial device technologies based on transition metal dichalcogenides (TMDs), wafer-scale, single-crystal continuous WS_2 monolayers are required. Powder vapor transport (PVT), which involves the evaporation of WO_3 and S powders in a heated tube furnace, has been successfully employed for the growth of WS_2 monolayer domains and films.[5,6] However, the low vapor pressure of WO_3 (~0.08 Torr at 1100 °C)[7] necessitates the use of furnace temperatures in excess of 900 °C to achieve appreciable metal source flux. Additionally, PVT lacks the flexibility to independently control and modulate the source partial pressure during growth. As a result of these constraints, metalorganic chemical vapor deposition (MOCVD), also referred to as gas source chemical vapor deposition, has emerged as a promising technique for wafer-scale synthesis of monolayer WS_2 as well as other TMD films.[8−10] MOCVD growth of polycrystalline WS_2 films was originally reported by Hoffman[11] and later Chung *et al.*[12] using tungsten hexacarbonyl ($W(CO)_6$) and hydrogen sulfide (H_2S). More recently, organo-chalcogen precursors including diethyl sulfide ($S(C_2H_5)_2$)[8,13] and di-*tert*-butyl sulfide ($(S(C_4H_9)_2)$)[14] have also been used, although simultaneous carbon deposition has been noted in cold-wall reactor geometries.[13]

Received: August 11, 2020
Accepted: January 11, 2021
Published: January 15, 2021

https://dx.doi.org/10.1021/acsnano.0c06750
ACS Nano 2021, 15, 2532−2541

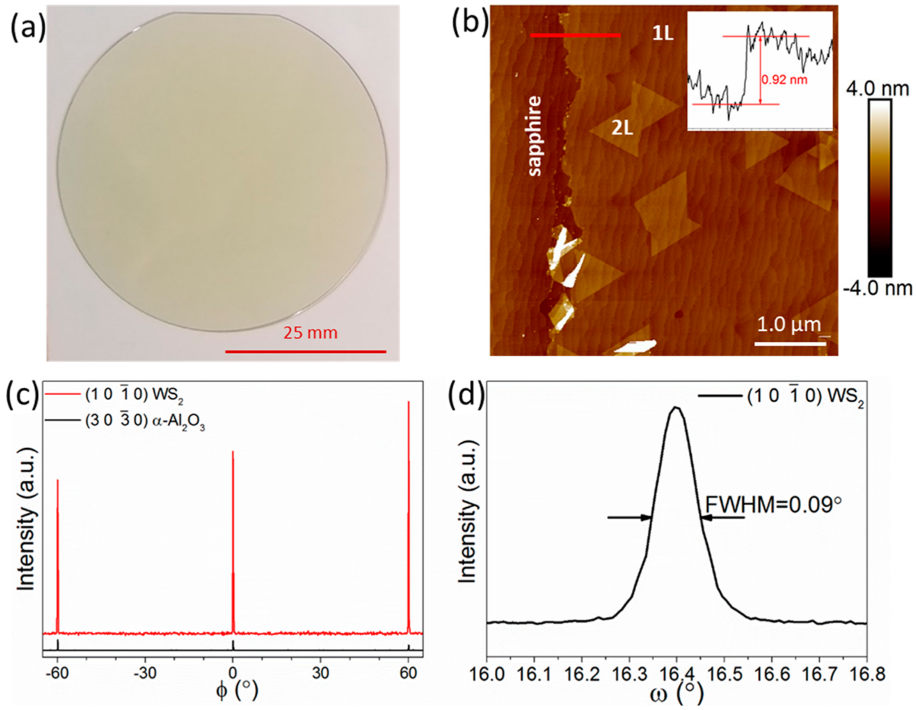

Figure 1. (a) Photograph of a WS_2 monolayer film deposited on a 2-inch *c*-plane sapphire substrate using a multistep process with varying temperature. (b) AFM topography micrograph of a WS_2 film showing a scratch at the left and monolayer coverage with some areas of bilayer growth. The inset shows the height profile along the red line in the top left corner showing a height difference of 0.92 nm. In-plane XRD of a WS_2 sample deposited using a variable-temperature multistep process, showing (c) a φ-scan of $\{10\bar{1}0\}$ and $\{30\bar{3}0\}$ planes of WS_2 and sapphire, indicating epitaxial growth, and (d) a ω-scan of $\{10\bar{1}0\}$ planes of WS_2, showing a low value of in-plane rotational twist.

MOCVD growth of coalesced TMD monolayer films on amorphous substrates such as oxidized Si and fused silica leads to randomly oriented domains bounded by high-angle grain boundaries, which serve as scattering centers for charge carriers and are generally undesired. Epitaxial growth on single-crystal substrates can potentially eliminate the formation of high-angle grain boundaries and is therefore of significant importance for electronic grade TMD films. *c*-Plane sapphire ((0001) α-Al_2O_3) is a promising substrate for epitaxial growth of WS_2 due to its crystallographic compatibility and good thermal and chemical stability. The lattice mismatch between WS_2 and sapphire is approximately 30% ($a_{\alpha\text{-Al2O3}}$ = 4.7597 Å; a_{WS2} = 3.1532 Å); nevertheless, the effective lattice mismatch can be significantly reduced assuming domain epitaxy (*i.e.*, three-unit cells of WS_2 match with two-unit cells of α-Al_2O_3). Epitaxial growth of MoS_2 on (0001) α-Al_2O_3 by PVT was initially demonstrated and explained with similar considerations.[15] It was shown that the energetically favorable epitaxial relation is $(10\bar{1}0)$ MoS_2 ∥ $(10\bar{1}0)$ α-Al_2O_3,[15] which allows the $\langle 10\bar{1}0\rangle$ vectors of (0001) α-Al_2O_3 and MoS_2 to be parallel and antiparallel.

In monolayer WS_2, as well as in other TMD materials, $\langle 10\bar{1}0\rangle$ and $\langle \bar{1}010\rangle$ are not equivalent directions, and domains with opposite directions are referred to as 0° and 60° (or 180°) rotated domains, antiphase domains, or inversion domains. Inversion domain boundaries (IDBs), which form upon coalescence of 0° and 60° domains, have a metallic character that introduces conducting channels in the semiconductor monolayer.[16] IDBs are further problematic for observation of spin and valley polarization which rely on transitions that occur at the K and −K points in the Brillouin zone.[17] The presence of 0° and 60° domains is readily apparent as oppositely oriented triangles for isolated domains formed on *c*-plane sapphire as reported for MoS_2 grown by PVT[15,18] and WSe_2 grown by MOCVD.[19] However, the presence of steps on the sapphire surface has been reported to induce alignment of isolated WSe_2[20] and $MoSe_2$[21] domains in PVT growth, providing a possible pathway to reduce or even eliminate IDBs in coalesced epitaxial TMD films.

In this work, we extend these approaches to demonstrate MOCVD growth of epitaxial, fully coalesced WS_2 monolayers on 2 in. diameter *c*-plane sapphire that exhibit a preferred crystallographic direction (herein referred to as unidirectional). A multistep variable-temperature growth process was necessary to reduce the in-plane rotational domain misorientation, as assessed by in-plane X-ray diffraction (XRD), and achieve fully coalesced monolayer films. Transmission electron microscopy (TEM) characterization reveals that the WS_2 monolayers are largely free of IDBs but instead consist of coalesced single-crystal regions with the same crystallographic direction separated by translational boundaries that arise from a slight lattice offset between coalescing domains. The microstructure and unidirectional nature of the monolayer are attributed to the high nucleation density along the sapphire surface steps. Growth conditions that preserve the aligned step morphology while promoting surface diffusion and lateral domain growth are necessary to reduce domain misorientation and achieve unidirectional growth. The results represent a promising step toward the realization of wafer-scale single-crystal WS_2 monolayer films using a process that can be readily extended to other materials in the TMD family.

https://dx.doi.org/10.1021/acsnano.0c06750
ACS Nano 2021, 15, 2532−2541

RESULTS AND DISCUSSION

Epitaxial growth of TMDs typically requires high substrate temperatures (>700 °C) to provide sufficient thermal energy to promote surface diffusion of metal-containing species.[5,15,19] Under these conditions, however, significant desorption of sulfur will occur due to its high vapor pressure;[22] consequently, an excess of chalcogen to metal precursor is required to maintain growth stoichiometry. These growth conditions also impact the epitaxial orientation of TMD domains on the *c*-plane sapphire surface as illustrated in this study. For WS_2, a multistep growth process (nucleation−ripening−lateral growth) previously developed for epitaxial growth of WSe_2 on sapphire was employed. Zhang *et al.*[19] used a constant growth temperature of 800 °C throughout the multistep process for WSe_2; however, for WS_2, variable temperatures yielded improved structural properties. Nucleation of WS_2 on sapphire was first carried out at 850 °C using $W(CO)_6$ and H_2S as precursors in a H_2 carrier gas, followed by ripening in H_2/H_2S for 20 min at 850 °C and 10 min at 1000 °C (see Materials and Methods and Figure S1). The $W(CO)_6$ precursor was then switched back into the reactor, and lateral growth was carried out at 1000 °C to enlarge the WS_2 domains and achieve a coalesced monolayer across the 2 in. sapphire wafer (Figure 1(a)). The WS_2 monolayer follows the morphology of the *c*-plane sapphire, which consists of undulations arising from surface steps (Figure 1(b)). A step height of 0.92 nm was measured across a scratch on the monolayer (Figure 1(b) inset), similar to the value previously reported for single-layer WS_2 flakes.[23] The step height value of 0.92 nm is larger than the spacing between the {0002} planes of 2H-WS_2, which is 0.62 nm,[24] and is attributed to the larger van der Waals gap between the film and sapphire substrate, as previously reported for MoS_2 and WSe_2 on sapphire.[25,26] The lateral growth time was 45 min for this sample, giving an effective growth rate of ∼1.6 monolayer/hour (monolayer + bilayer). It should be noted that this growth rate is significantly faster than the growth rates of ∼0.04−0.05 monolayer/hour reported for MOCVD WS_2 films grown in hot wall reactor configurations using organo-chalcogen sources.[8,14] Figure 1(c) shows in-plane XRD φ-scans of the $\{10\bar{1}0\}$ and $\{30\bar{3}0\}$ planes of WS_2 and α-Al_2O_3, respectively. The existence of WS_2 peaks separated by 60° from each other and the coincidence of the WS_2 peak positions with those of α-Al_2O_3 indicates that the epitaxial relationship is $(10\bar{1}0)$ WS_2 ∥ (100) α-Al_2O_3. Figure 1(d) shows the in-plane XRD ω-scan of the WS_2 $(10\bar{1}0)$ plane. The full-width at half-maximum (FWHM) observed for this peak is 0.09°, indicating a low degree of in-plane rotational misorientation or twist. The use of a lower temperature (850 °C) for nucleation and ripening enables epitaxial growth of WS_2 without excessive roughening of the sapphire, while an increased temperature (1000 °C) during lateral growth leads to a narrower FWHM (Figure S2). Triangular-shaped bilayer domains are present on the monolayer and range in coverage from ∼22% to ∼17% from the center to the edge of the wafer, respectively (Figure S3). Additional AFM and SEM images, illustrating the surface morphology and uniformity across the entire 2 in. wafer, are included in Figure S4. Raman spectroscopy using 532 and 633 nm laser lines was also used to assess the thickness of the WS_2 films on sapphire. However, the Raman peak positions and separation were found to be impacted by residual stress in the WS_2 on the growth substrate (see Figure S5) and therefore could not be used to accurately assess layer number. Comparison of the ultra-low-frequency (ULF) Raman spectra of WS_2 with different thicknesses, however, provides further evidence of the monolayer nature of the films, as indicated in Figure S6.

The growth rate was also found to impact the microstructure of the WS_2 monolayer. AFM images of WS_2 films deposited using growth rates of 1.3 and 3 monolayer/hour are shown in Figure 2(a) and (b), respectively. At 3 monolayers/hour, the bilayer coverage is further reduced to 0.77% at the center and 0.22% at the edge for this sample (Figure S7). TEM was used to study the microstructure of the WS_2 monolayers which were removed from the sapphire growth substrates by a water-based transfer method and transferred onto Cu TEM grids (see Materials and Methods). Composite dark-field (DF) TEM images shown in Figure 2(c,d) were prepared by stitching together a series of DF images (shown in Figure S8) such that the structural properties of the WS_2 were revealed over an area comparable to that of the AFM scans. The selected area electron diffraction (SAED) pattern of the coalesced WS_2 films (Figure S8(a,d)) indicates that they are single-crystalline; that is, they contain a single set of spots with the 6-fold symmetry of the 2H WS_2 crystal lattice. In the DF-TEM images, Figure 2(c,d), the white areas correspond to the bilayer regions. The large circular features present in the composite images are artifacts arising from the holes in the carbon coating of the TEM grid. Small black features are also present in the DF-TEM images and are associated with pinholes in the monolayer (see Figure S8(g)) that may arise from incomplete film coalescence or defects introduced during transfer. Within the WS_2 monolayer, two contrasting gray regions (designated region 1 and region 2) are present (Figure 2(c,d)). It should be noted that these DF-TEM features were observed in every WS_2 film studied that was grown using the multistep process (10 films from different growth runs). To determine the structure of the two regions and their boundaries, the DF-TEM maps were correlated with atomic-resolution ADF-STEM

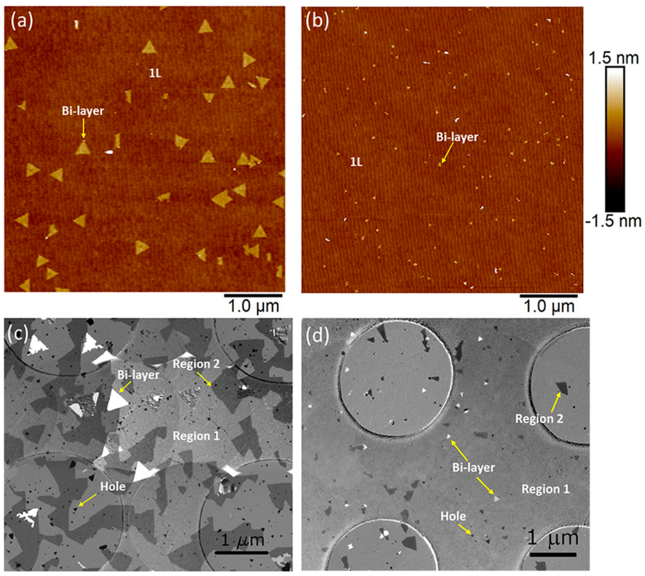

Figure 2. (a) AFM micrograph of WS2 deposited at a growth rate of 1.3 monolayer/min. (b) AFM micrograph of films deposited at a growth rate of 3 monolayer/min. (c) Composite dark-field TEM map of the film corresponding to (a). (d) Composite dark-field TEM map of the film corresponding to (b).

https://dx.doi.org/10.1021/acsnano.0c06750
ACS Nano 2021, 15, 2532−2541

imaging. The details of this correlation are discussed in the Supporting Information (Figure S9), the Materials and Methods section, and a related publication.[27] DF-TEM images of the WS_2 monolayer from the center and edge of the wafer are shown in Figure S10 to highlight the microstructural uniformity of the film across the entire 2 in. diameter area.

Figure 3(a) is a low-magnification dark-field image of an area containing the different regions of contrast. Within a given region, the high-resolution atomic structure is single crystalline (Figure 3(b)). At the interface between two regions, Figure 3(c), a line defect is present. Analysis of this defect (Figure 3(d)) reveals no significant angular rotation of the lattice across the boundary and, furthermore, that the lattice orientation is identical on both sides, indicating a lack of an inversion domain boundary. Instead, the white dashed line in Figure 3(d) shows that there is a translational offset between the two regions separated by the line defect. A schematic of the atomic structure of WS_2 has been superimposed on the high-resolution image to aid visualization. This result is distinct from a previous report of the contrast difference in DF-TEM in MoS_2, which was attributed to inversion domains that arise due to coalescence of 0° and 60° oriented domains.[28] The line defects in the WS_2 monolayer instead arise from coalescing domains that have the same crystallographic direction (referred to as unidirectional) but lattices that are offset from one another by less than a unit cell.

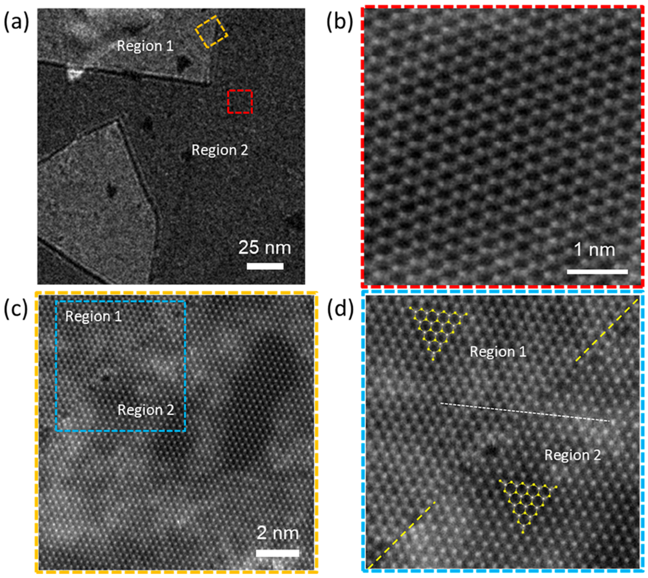

Figure 3. (a) Low-magnification DF-TEM image showing the two regions of differing contrast. High-resolution images showing (b) the 2H WS_2 matrix structure (darker gray region in (a)), (c) a region containing the two contrasting areas, and (d) higher resolution atomic structure image showing the line defect separating the two regions of different contrast but same orientation. In (d) the grain boundary is highlighted by a dashed yellow line. A dashed white line across the boundary shows the translational offset between the two regions. The same orientation is confirmed by the relative positions of W and S, which is highlighted by the superimposed WS_2 structure.

The line defects can be described as translational boundaries, and detailed analysis of their structure and geometry indicates that they arise from coalescence of WS_2 domains with well-defined edge orientations. Because these edges do not follow the zigzag edge as expected from previous studies on isolated domains obtained using powder vaporization, they give rise to the irregular shapes within the coalesced monolayer in the DF-TEM images.[27] Translational boundaries are the dominant type of line defect present in all of the WS_2 monolayers examined, in contrast to prior reports for MoS_2[18] and WSe_2 monolayers[19] grown on sapphire where IDBs were predominant. In the present case, the contrast in the DF-TEM images between regions separated by a translational boundary is the result of excitation error, which arises due to small tilts in the domains, caused by stitching. Figure S11 includes an example series of simulated diffraction patterns showing the intensity variations of diffraction spots with sample tilt, tracking how the spot intensity ratios change. Two grains with different tilts will contribute unequally to the intensity of their overlapping diffraction spot, giving rise to the type of DF-TEM contrast observed experimentally. The difference in 2S column intensity on both sides of the translational boundaries (Figure 3 c,d) observed in the ADF-STEM images is also consistent with the two grains not being aligned identically relative to the electron beam. Tilt has been previously observed in TMDs at misoriented GBs and has been reported to occur due to the local strain resulting from the GBs.[29] Although sulfur atoms ($Z = 16$) have much lower ADF-STEM intensity than tungsten atoms ($Z = 74$), it was possible to unambiguously identify that the WS_2 film has the 2H crystal structure on both sides of the GB, with the same $x-y$ orientation.

Despite the unidirectional nature in the monolayer, the AFM images in Figures 1(b) and 2(a) show that the bilayer domains exhibit a variety of orientations including 0° and 60° oriented domains. Oppositely oriented triangles are commonly observed for epitaxial growth of TMDs on van der Waals surfaces such as graphene since there is no energetic difference between the orientations.[30,31] Furthermore, bilayers are expected to nucleate at defects in the underlying monolayer such as the translational boundaries or point defects which can give rise to a wider range of orientations. Consequently, it is not possible to determine the orientation of the monolayer based on the bilayer orientation, as demonstrated in Figure 2, where bilayers of variable orientations are present on single-orientation monolaye WS_2.

The absence of inversion domains in the WS_2 monolayer is believed to result from the stepped structure of the *c*-plane sapphire surface and the multistep process employed for layer growth. Figure 4 shows the surface morphology of the sapphire and the WS_2 at different growth temperatures. The *c*-plane sapphire surface, as received, consists of steps aligned along the $[11\bar{2}0]$ direction with an average terrace spacing of ~70−100 nm (Figure 4(a)). After 30 s of nucleation at 850 °C and 20 min of ripening (850−950 °C), the surface consists of small (≤10 nm) WS_2 clusters that exhibit aggregation relative to one another (Figure 4(b)). During ripening, the clusters are expected to be mobile, similar to that reported for WSe_x clusters on sapphire,[19] and consequently can diffuse to the step edges on the sapphire. The steps may induce a preferred orientation in the WS_2 domains similar to what has been observed for WSe_2[20] and $MoSe_2$[21] grown on sapphire by PVT. In fact, a theoretical model recently proposed for epitaxial growth of 2D materials[32] predicts unidirectional alignment of the zigzag edge of TMD domains parallel to $\langle 11\bar{2}0\rangle$ direction on vicinal (0001) Al_2O_3 due to the impact of high-index step edges, consistent with our experimental observations. After an

https://dx.doi.org/10.1021/acsnano.0c06750
ACS Nano 2021, 15, 2532−2541

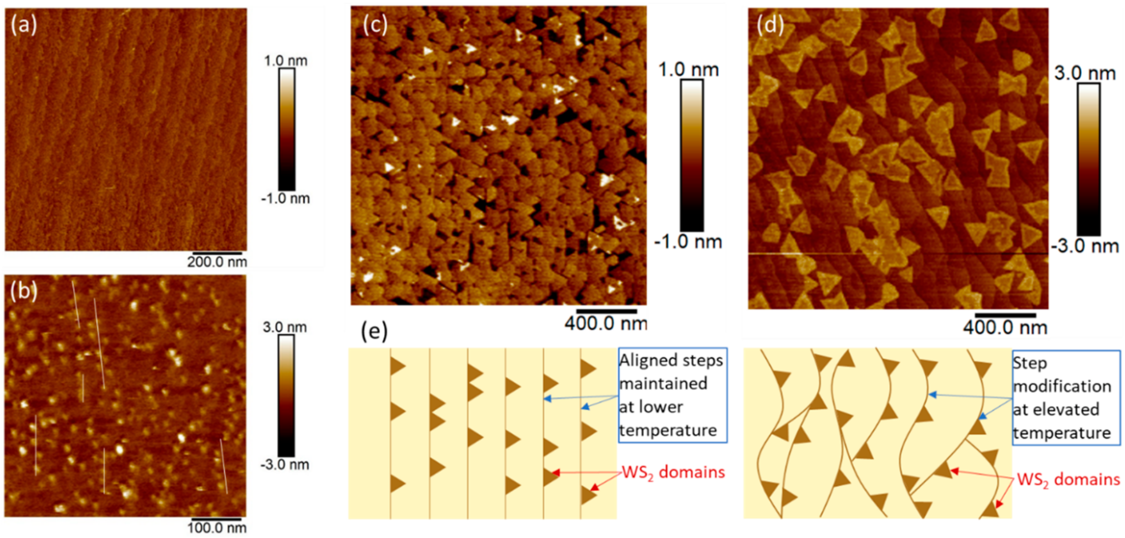

Figure 4. AFM micrographs of (a) as-received sapphire substrate. (b) WS_2 clusters deposited after nucleation and ripening stage at 850 °C. White lines are provided as a guide to the eye. (c) WS_2 monolayer morphology after 10 min of lateral growth at 1000 °C, when nucleation and ripening were carried out at 850 °C. (d) Isolated WS_2 domains obtained at a constant-temperature process at 1000 °C. (e) Schematic shows the top view of the substrate. Well-aligned domains oriented by the step edges are observed when the surface step structure is maintained by performing the early stages (nucleating and ripening) at the lower temperature of 850 °C. High-temperature exposure starting at the beginning of the process distorts the surface step structure, resulting in WS_2 domains nucleating in various orientations.

additional 10 min of lateral growth at 1000 °C (Figure 4(c)), a high density of WS_2 domains, ∼100−200 nm in size, are present and the film is nearly fully coalesced. The domain edges are clearly visible in this case, which highlights the oriented nature of the domains. The step-guided nucleation imparts a preferred orientation to the domains, which is maintained during lateral growth at 1000 °C. Many of the small domains near one another merge together seamlessly during coalescence to form much larger, single-crystalline regions, as shown by the uniform contrast over micron-sized regions in Figure 2(b,d). Such regions of coalescence sometimes can be located by arrays of metal vacancies in the WS_2 monolayer,[33] which remain after multiple small, coherent domains coalesce, leaving behind arrays of point defects. On a larger scale, the lattice mismatch between WS_2 and sapphire creates a translational boundary like that shown in Figure 3(c,d) when these locally fused single-crystal regions coalesce slightly offset from each other.

In order to impart a preferred orientation to the WS_2 domains, the sapphire step structure must be preserved at the nucleation step. Figure 4(d) shows the WS_2 domain morphology when the entire process is carried out at 1000 °C with 5 min of lateral growth. At a higher temperature, the WS_2 domain density and surface coverage are lower due to a reduced nucleation density and enhanced precursor desorption. Under these conditions, the sapphire surface is modified by high-temperature exposure, resulting in an increase in the terrace width as well as undulations in the step alignment. This gives rise to increased misorientation of domains as nucleation occurs at step edges that are not as well aligned. These multioriented domains give rise to multiple peaks in in-plane XRD as shown in Figure S2(b).

A schematic illustration of the proposed mechanism is shown in Figure 4(e). When nucleation occurs on a substrate with well-defined parallel steps, unidirectional domains are formed. As the domains coalesce, larger regions with a slight lateral misalignment merge, forming translational boundaries. When the substrate is exposed to high temperatures, which causes step distortion, nucleation may still occur at step edges; however, the step edges are no longer parallel. Consequently, the WS_2 domains exhibit multiple orientations. These observations indicate that the route to achieving a unidirectional TMD film is by maintaining a well-defined regular surface step structure during the nucleation process. Once a preferred orientation of domains is established, high-temperature lateral growth helps to improve the structural properties, as evidenced by a reduction in the in-plane XRD FWHM (Figure 1(c,d)). The domain alignment and the resulting microstructure of the monolayer are therefore expected to be dependent on the size and density of the initial WS_x clusters and WS_2 domains, the step structure of the sapphire, and growth conditions. As shown in Figure 2(c,d), the density of translational boundaries (as measured by the regions of contrast) is dependent on growth rate. At a higher monolayer growth rate, the nucleation density would be higher and hence the WS_2 domain size would be smaller, enabling migration and alignment of domains during coalescence, resulting in larger single-crystalline regions. These results demonstrate that large single-epitaxial TMD monolayers can be obtained even when the initial domain density is high as is typically the case for MOCVD- and MBE-grown material. This observation contrasts with PVT, where a low nucleation density favors the formation of large single-crystalline domains.[34] Both of these approaches can result in a single-crystalline film. However, the presence of steps on the substrate surface enables small domains to orient and coalesce into a unidirectional wafer-scale film.

The optical and transport properties of fully coalesced WS_2 monolayers were characterized to assess the quality of the material. Photoluminescence measurements were obtained over the temperature range from 80 to 280 K. This is especially useful, as the defect-bound exciton intensity was reported to increase as the temperature decreases from 250 to 77 K,[35] indicating that the intensity of defect-bound exciton emission at low temperatures can be used as a measure of film quality. Figure 5(a) shows that the PL peak for as-grown WS_2

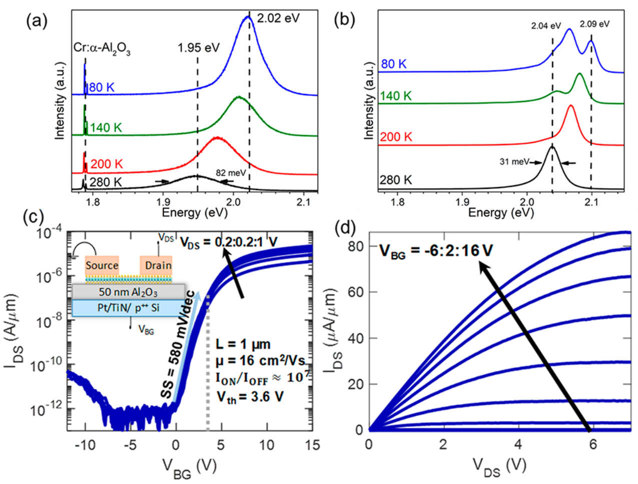

Figure 5. Temperature-dependent PL for (a) as-grown WS_2 on a sapphire substrate and (b) WS_2 transferred onto a SiO_2/Si substrate. (c) Back-gated transfer characteristics for a WS_2 FET with the key transistor parameters and the device schematic shown in the inset. The drain current (I_{DS}) *versus* back-gate voltage (V_{BG}) for drain voltages (V_{DS}) ranging from 0.2 to 1 V is used to find the field effect mobility (μ), subthreshold slope (SS), threshold voltage (V_{th}), and ON−OFF ratio ($I_{ON/OFF}$). (d) Output characteristics of the WS_2 FET. The maximum saturation-current is extracted from the output characteristics.

on sapphire shifts from 1.95 eV at 280 K to 2.02 eV when the temperature is reduced to 80 K. At 80 K, several spots on the sample were selected to perform PL measurements that showed variation of the peak position between 2.02 and 2.04 eV. Note that the low-intensity sharp peak visible at 1.78 eV originates from a Cr impurity in α-Al_2O_3.[36] Negligible defect-bound exciton emission was observed in the low-temperature PL, suggesting that the MOCVD-grown WS_2 monolayer has good optical quality. Low-temperature PL measurements were also carried out on a WS_2 monolayer transferred to a SiO_2/Si substrate (Figure 5(b)). The 280 K PL emission maximum shifted to higher emission energy (2.04 eV), and the FWHM decreased from 82 meV to 31 meV. The FWHM of the exciton emission reported in the literature for WS_2 exfoliated flakes at room temperature is approximately 30 meV,[37] comparable to the FWHM value observed for the transferred WS_2 film. The shift in PL peak position toward higher emission energies upon transfer has previously been observed for PVT-synthesized TMD films on sapphire, SiO_2/Si, and fused silica and was attributed to the relaxation of high-temperature growth-induced strain.[38] The transferred film also does not show prominent emission related to defect-bound excitons, suggesting that the optical quality of the material is preserved after the transfer. However, additional peaks emerge in the transferred sample at low temperature that can be attributed to trion (highest intensity peak) and biexciton emission, visible as a shoulder on the lower energy side from the trion.[39] The origin of the peaks was determined by excitation laser power dependent measurements, as shown in Figure S12. The PL spectra obtained at different powers at 80 K were fitted to extract the peak positions, and the power dependence was determined.[39,40]

Electrical characterization of the WS_2 films was also carried out to assess the transport properties. Back-gated field-effect transistors (FETs) were fabricated (see Materials and Methods section) after transferring the WS_2 film to 50 nm aluminum oxide (Al_2O_3) with Pt/TiN/p^{++} Si as the substrate and a back-gate electrode as shown in the device schematic in the inset of Figure 5(c) and Figure S13. Figure 5(c) shows the transfer characteristics of a typical WS_2 FET, *i.e.*, the drain current (I_{DS}) *versus* the back-gate voltage (V_{BG}) for different drain voltages (V_{DS}). Additional transfer characteristics and statistics of 10 devices fabricated across a 1 cm × 1 cm sample region are included in Figure S14, demonstrating a variation of less than ±20%. Clearly, the monolayer WS_2 FET shows dominant electron transport along with a weak hole branch consistent with other reports.[41,42] Key FET performance metrics such as the field effect mobility (μ_{FE}), subthreshold slope (SS), threshold voltage (V_{th}), and ON−OFF ratio ($I_{ON/OFF}$) were evaluated. A μ_{FE} of 16 cm^2/(V s) was extracted from the peak transconductance using the equation $\mu_{FE} = g_m L / C_{ox} W V_{DS}$, where g_m is the transconductance $\left(g_m = \frac{\partial I_{DS}}{\partial V_{GS}}\right)$, L is the channel length, C_{ox} is the oxide thickness, and W is the width of the channel. V_{th} was found to be 3.6 V using the constant-current method (at 100 nA/μm), and SS was found to be 580 mV/decade. A high $I_{ON/OFF}$ of approximately 10^7 is also measured. Figure 5(d) demonstrates the output characteristics, *i.e.*, I_{DS} *versus* V_{DS} for different V_{BG}. A high saturation current of 86 μA/μm was measured at a V_{BG} of 16 V and drain voltage (V_{DS}) of 7 V, corresponding to a carrier density of 1.13×10^{13} cm^{-2}. The mobilities reported were also comparable to the values in the literature[8,43] for WS_2 films synthesized on SiO_2 or Au foils by gas-source or PVT processes. The promising electrical performance further supports the high material quality of the wafer-scale MOCVD-grown WS_2 film.

CONCLUSIONS

The epitaxial growth of unidirectional WS_2 monolayer films on a 2 in. *c*-plane sapphire wafer was demonstrated using a multistep MOCVD growth process. By employing a variable-temperature process and controlling the growth rate, fully coalesced monolayer WS_2 with low in-plane rotational twist (0.09°) and minimal bilayer coverage (<1%) was demonstrated across the entire 2 in. diameter wafer. TEM characterization of the WS_2 monolayer reveals micron-size single-crystal regions with the same crystallographic direction bounded by translational line defects and negligible inversion domains. The unidirectional nature of the WS_2 is attributed to the presence of parallel steps on the sapphire surface, which serve to induce a preferred alignment. Modification of the sapphire step structure at elevated temperatures leads to an increase in domain misorientation. The optical and electrical properties of the WS_2 monolayers were characterized for films transferred off the sapphire. Clearly resolved neutral and charged exciton peaks were observed in the photoluminescence spectra obtained at 80 K with no prominent defect-related emission. Back-gated WS_2 FETs also exhibit a high drive current and a high $I_{ON/OFF}$. This work demonstrates the possibility of producing wafer-scale single-crystal TMD monolayers by MOCVD with properties approaching those of exfoliated flakes.

https://dx.doi.org/10.1021/acsnano.0c06750
ACS Nano 2021, 15, 2532−2541

MATERIALS AND METHODS

Synthesis. A cold-wall, horizontal, low-pressure MOCVD reactor[44] was employed for the growth of WS_2 films (Supporting Information Figure S15). Tungsten hexacarbonyl ($W(CO)_6$) and hydrogen sulfide (H_2S) were used as the tungsten and sulfur precursors, respectively, with hydrogen (H_2) as the carrier gas. $W(CO)_6$ was kept in a stainless-steel bubbler held at a constant temperature (10 °C) and pressure (760 Torr), and H_2 gas was passed through it to transport the precursor vapor to the reactor. The inlet gas flow rates of $W(CO)_6$ and H_2S were in the range of 6.4×10^{-5} to 1.3×10^{-4} sccm (7×10^{-7} to 14×10^{-7}Torr) and 160−400 sccm (1.7−4.4 Torr), respectively. Additional H_2 gas was introduced to achieve a total gas flow rate of 4500 sccm through the reactor. Two-inch double-side polished epi-ready *c*-axis oriented sapphire ((0001) α-Al_2O_3) wafers were used as substrates for the growth. No additional treatment was performed on the as-received wafers. The wafers were placed on the SiC-coated graphite susceptor rotating disc. The reactor pressure was kept constant at 50 Torr. Prior to growth, sapphire wafers were held in H_2 at a temperature of 850 or 1000 °C, depending on the growth, for 10 min to remove residual surface contaminants. Growth was initiated by simultaneously introducing the precursors into the inlet gas stream.

For the growth of WS_2, a multistep process (nucleation, ripening, lateral growth) was employed similar to that reported by X. Zhang *et al.* for the growth of WSe_2.[19] Figure S1 in the Supporting Information illustrates the general recipe used for the growth. For the initial experiments, a multistep process at constant temperature was implemented, whereas later experiments were conducted using varying temperatures for the different steps. First, at a temperature of 850 °C, both H_2S and $W(CO)_6$ were introduced for 30 s with $W(CO)_6$ and H_2S flow rates of 1.3×10^{-4} sccm and 400 sccm, respectively, to form the initial WS_2 nuclei on the substrate. In the ripening step, the $W(CO)_6$ was then switched out to bypass the reactor while the flow of H_2S continued into the reactor at a constant rate for 20 min (30 min for initial experiments at constant temperature) to allow surface diffusion and ripening of the WS_2 domains to occur. The temperature was then ramped from 850 to 1000 °C and held for 10 min. After the ripening stage, $W(CO)_6$ was reintroduced into the reactor at half the flow rate (6.4×10^{-5} sccm) compared to that of the nucleation step for times ranging from 10 to 45 min to allow the domains to grow laterally in size and coalesce. After growth, the layers were annealed in H_2S flow for an additional 10 min at the growth temperature and were then cooled to 300 °C under a flow of H_2 and H_2S to avoid WS_2 decomposition. After the temperature decreased below 200 °C, the H_2 flow was stopped, the reactor was evacuated to 3×10^{-3} Torr, and a reactor purging procedure using N_2 was initiated to remove any residual H_2S from the reactor before the sample was removed. The sample was then unloaded from the reactor into a N_2-purged glovebox to avoid exposing the sample and reactor directly to atmospheric moisture and oxygen. Between characterization studies, the samples were stored in a N_2-ventilated cabinet to reduce further sample degradation.

Film Transfer Details. The films were transferred from sapphire for TEM, low-temperature photoluminescence (PL), and electrical characterization. The typical transfer procedure involves coating an as-grown sample with poly(methyl methacrylate) (PMMA) using a spin-coater in two steps: 500 rpm for 15 s followed by 4500 rpm for 45 s. After the PMMA coating cures overnight, the sample edges are scratched to assist delamination, and the sample is then immersed into 1 M NaOH solution in DI water and held at 90 °C for 15−20 min. NaOH helps delaminate the WS_2 film from the substrate, and when it does, the PMMA+WS_2 film assembly floats on the surface of the NaOH solution. The assembly is then transferred to a DI water bath for 10 min for rinsing. This step is then repeated three more times to ensure the complete removal of residual NaOH from the previous step. The assembly is then fished out using a 3 mm diameter Cu Quantifoil TEM grid, SiO_2/Si, and 50 nm of Al_2O_3 with Pt/TiN/p^{++} Si substrate for TEM, PL and electrical characterization, respectively. In the case of TEM, transfer is done so that the Quantifoil side touches the WS_2 film. The PMMA+WS_2 film + TEM grid assembly is heated at 50 °C for 10 min and at 70 °C for 10 more minutes before placing it into an acetone bath for the removal of PMMA film. The TEM grid, which has the WS_2 film on the Quantifoil side, is then transferred into an alcohol (methanol or isopropanol) bath to remove acetone residue. Finally, the grid is heated at 70 °C on a hot plate for 10 min. The same procedure is followed for the transfer of the films to the other substrates.

Material structural characterization. A Bruker Icon atomic force microscope (AFM) was used to study the surface morphology, domain size, coverage and thickness of the deposited layers. Scanasyst air probe AFM tips with a nominal tip radius of ∼2 nm and spring constant of 0.4 N/m were employed for the measurements, and images were collected using peak-force tapping mode. To measure the thickness of the deposited films, samples were lightly scratched using a blunt tweezer to remove a portion of the weakly bonded WS_2 film without damaging or scratching the sapphire surface.

A PANalytical MRD diffractometer with 5-axis cradle was employed for X-ray diffraction characterization of WS_2 films. A standard Cu anode X-ray tube operated at 40 kV accelerating voltage and 45 mA filament current was used to generate X-rays. As primary optics, a mirror with 1/4° slit and Ni filter was used to discriminate the Cu K_β line. On the diffracted beam side, an 0.27° parallel plate collimator with 0.04 rad Soller slits with PIXcell detector in open detector mode were employed. Samples were positioned in such a way that the sample surface was ∼2−4° away from the X-ray incidence plane. Such a configuration allows measurement of diffraction caused by the (hki0) planes to determine the in-plane epitaxial relation of the film with respect to a substrate, as previously reported.[45]

A Zeiss Merlin electron microscope was used for acquiring the scanning electron micrographs. An accelerating voltage of 3 kV and a working distance of 3 mm was used with the in-lens detector to capture the images.

Raman measurements were performed using a HORIBA LabRAM HR Evolution Raman microscope with laser wavelengths of 532 and 633 nm. For Raman measurements, a grating with 1800 grooves per mm was employed. Raman WS_2 signature positions as well as the position and intensity of the near bandgap emission in PL from WS_2 were used to confirm the formation of mainly monolayer films.

Temperature-dependent PL measurements were performed under 488 nm laser excitation using a Renishaw inVia Raman microscope. A Linkam THMS600 optical stage was used as the sample holder during PL spectra acquisition. All measurements were performed in nitrogen atmosphere.

The deposited WS_2 films were imaged using various TEM techniques to reveal the structure of the films at the atomic level. Annular dark-field scanning TEM (ADF-STEM) imaging was performed on an FEI Titan3 G2 operating at an accelerating voltage of 80 kV with a probe convergence angle of 30 mrad and probe current of 70 pA. Dark-field (DF-) TEM imaging was performed on a FEI Talos F200X using a 10 μm objective aperture to select a {100} diffraction spot. DF-TEM images were acquired for 30 s each. Composite DF-TEM images were prepared for the WS_2 to reveal the microstructure' on a larger scale. The composite DF-TEM map is built from individual micrographs using GIMP 2 image processing software to adjust the contrast between different micrographs and within a single micrograph, in which areas with free-standing film are accompanied by areas where the film is supported by the carbon TEM grid. The composite image preparation used here is similar to that reported by P. Y. Huang et al. for graphene.[46]

Electrical characterization. The as-grown WS_2 on sapphire substrate is transferred to a substrate with 50 nm Al_2O_3 with Pt/TiN/p^{++} Si as the back-electrode stack. Electron beam (e-beam) lithography (Vistec EBPG5200) is used for the isolation step to define the channel dimensions. After the electron beam exposure and the develop step, SF_6 etch (PT Dual Etch Versalock) is done to define the device area. Then the source and drain electrodes are defined using another e-beam lithography step to obtain a channel length (L) of 1 μm. A 40 nm Ni/30 nm Au stack is deposited through e-beam

https://dx.doi.org/10.1021/acsnano.0c06750
ACS Nano 2021, 15, 2532−2541

evaporation (Temascale FC2000) to obtain the final back-gated FET device structure. Following the device fabrication, the electrical characterization was carried out at room temperature in high vacuum ($\sim 10^{-5}$ Torr) in a Lakeshore CRX-VF probe station using a Keysight B1500A parameter analyzer.

ASSOCIATED CONTENT

Supporting Information

The Supporting Information is available free of charge at https://pubs.acs.org/doi/10.1021/acsnano.0c06750.

> Additional details on the growth scheme, in-plane X-ray diffraction data, wafer-scale uniformity, Raman, PL, TEM results, and electrical characterization data (PDF)

AUTHOR INFORMATION

Corresponding Authors

Tanushree H. Choudhury − *2D Crystal Consortium-Materials Innovation Platform (2DCC-MIP), Materials Research Institute, The Pennsylvania State University, University Park, Pennsylvania 16802, United States;* orcid.org/0000-0002-0662-2594; Email: tuc21@psu.edu

Joan M. Redwing − *2D Crystal Consortium-Materials Innovation Platform (2DCC-MIP), Materials Research Institute and Department of Materials Science and Engineering, The Pennsylvania State University, University Park, Pennsylvania 16802, United States;* orcid.org/0000-0002-7906-452X; Email: jmr31@psu.edu

Authors

Mikhail Chubarov − *2D Crystal Consortium-Materials Innovation Platform (2DCC-MIP), Materials Research Institute, The Pennsylvania State University, University Park, Pennsylvania 16802, United States;* orcid.org/0000-0002-4722-0321

Danielle Reifsnyder Hickey − *2D Crystal Consortium-Materials Innovation Platform (2DCC-MIP), Materials Research Institute and Department of Materials Science and Engineering, The Pennsylvania State University, University Park, Pennsylvania 16802, United States;* orcid.org/0000-0002-8962-1473

Saiphaneendra Bachu − *Department of Materials Science and Engineering, The Pennsylvania State University, University Park, Pennsylvania 16802, United States;* orcid.org/0000-0001-9898-7349

Tianyi Zhang − *Department of Materials Science and Engineering, The Pennsylvania State University, University Park, Pennsylvania 16802, United States;* orcid.org/0000-0002-8998-3837

Amritanand Sebastian − *Department of Engineering Science and Mechanics, The Pennsylvania State University, University Park, Pennsylvania 16802, United States;* orcid.org/0000-0003-4558-0013

Anushka Bansal − *Department of Materials Science and Engineering, The Pennsylvania State University, University Park, Pennsylvania 16802, United States;* orcid.org/0000-0003-4340-362X

Haoyue Zhu − *2D Crystal Consortium-Materials Innovation Platform (2DCC-MIP), Materials Research Institute, The Pennsylvania State University, University Park, Pennsylvania 16802, United States*

Nicholas Trainor − *Department of Materials Science and Engineering, The Pennsylvania State University, University Park, Pennsylvania 16802, United States*

Saptarshi Das − *Department of Materials Science and Engineering and Department of Engineering Science and Mechanics, The Pennsylvania State University, University Park, Pennsylvania 16802, United States;* orcid.org/0000-0002-0188-945X

Mauricio Terrones − *Department of Materials Science and Engineering, Department of Chemistry, and Department of Physics, Center for 2-Dimensional and Layered Materials, The Pennsylvania State University, University Park, Pennsylvania 16802, United States;* orcid.org/0000-0003-0010-2851

Nasim Alem − *2D Crystal Consortium-Materials Innovation Platform (2DCC-MIP), Materials Research Institute and Department of Materials Science and Engineering, The Pennsylvania State University, University Park, Pennsylvania 16802, United States;* orcid.org/0000-0003-0009-349X

Complete contact information is available at: https://pubs.acs.org/10.1021/acsnano.0c06750

Author Contributions

#M.C. and T.H.C. have contributed equally.

Notes

The authors declare no competing financial interest.

ACKNOWLEDGMENTS

Primary financial support for this work was provided by the National Science Foundation (NSF) through the 2D Crystal Consortium−Materials Innovation Platform (2DCC-MIP) under NSF cooperative agreement DMR-1539916. D.R.H., S.B., and N.A. acknowledge additional support from an NSF CAREER grant (DMR-1654107). T.Z. and M.T. acknowledge the financial support of the Air Force Office of Scientific Research (AFOSR) through grant FA9550-18-1-0072. The work of S.D. and A.S. was partially supported by Army Research Office through Cooperative Agreement Grant W911NF1920338 and Air Force Office of Scientific Research (AFOSR) through the Young Investigator Program Grant FA9550-17-1-0018. This work utilized resources provided by the NSF-MRSEC-sponsored Materials Characterization Lab at Pennsylvania State University.

REFERENCES

(1) Li, Y.; Li, X.; Yu, T.; Yang, G.; Chen, H.; Zhang, C.; Feng, Q.; Ma, J.; Liu, W.; Xu, H.; Liu, Y.; Liu, X. Accurate Identification of Layer Number for Few-Layer WS2 and WSe2 *via* Spectroscopic Study. *Nanotechnology* **2018**, *29* (12), 124001.

(2) Iqbal, M. W.; Iqbal, M. Z.; Khan, M. F.; Shehzad, M. A.; Seo, Y.; Park, J. H.; Hwang, C.; Eom, J. High-Mobility and Air-Stable Single-Layer WS2 Field-Effect Transistors Sandwiched between Chemical Vapor Deposition-Grown Hexagonal BN Films. *Sci. Rep.* **2015**, *5*, 10699.

(3) Zhu, B.; Zeng, H.; Dai, J.; Gong, Z.; Cui, X. Anomalously Robust Valley Polarization and Valley Coherence in Bilayer WS2. *Proc. Natl. Acad. Sci. U. S. A.* **2014**, *111* (32), 11606−11611.

(4) Xiao, R.; Lan, C.; Li, Y.; Zeng, C.; He, T.; Wang, S.; Li, C.; Yin, Y.; Liu, Y. High Performance van der Waals Graphene−WS2−Si Heterostructure Photodetector. *Adv. Mater. Interfaces* **2019**, *6* (24), 1901304.

(5) Kang, K. N.; Godin, K.; Yang, E. H. The Growth Scale and Kinetics of WS2Monolayers under Varying H2 Concentration. *Sci. Rep.* **2015**, *5*, 13205.

(6) Lan, C.; Zhou, Z.; Zhou, Z.; Li, C.; Shu, L.; Shen, L.; Li, D.; Dong, R.; Yip, S.; Ho, J. C. Wafer-Scale Synthesis of Monolayer WS2 for High-Performance Flexible Photodetectors by Enhanced Chemical Vapor Deposition. *Nano Res.* **2018**, *11* (6), 3371−3384.
(7) Stull, D. R. Vapor Pressure of Pure Substances. Organic and Inorganic Compounds. *Ind. Eng. Chem.* **1947**, *39* (4), 517−540.
(8) Kang, K.; Xie, S.; Huang, L.; Han, Y.; Huang, P. Y.; Mak, K. F.; Kim, C. J.; Muller, D.; Park, J. High-Mobility Three-Atom-Thick Semiconducting Films with Wafer-Scale Homogeneity. *Nature* **2015**, *520* (7549), 656−660.
(9) Eichfeld, S. M.; Hossain, L.; Lin, Y. C.; Piasecki, A. F.; Kupp, B.; Birdwell, A. G.; Burke, R. A.; Lu, N.; Peng, X.; Li, J.; Azcatl, A.; McDonnell, S.; Wallace, R. M.; Kim, M. J.; Mayer, T. S.; Redwing, J. M.; Robinson, J. A. Highly Scalable, Atomically Thin WSe2 Grown *via* Metal-Organic Chemical Vapor Deposition. *ACS Nano* **2015**, *9* (2), 2080−2087.
(10) Chiappe, D.; Ludwig, J.; Leonhardt, A.; El Kazzi, S.; Nalin Mehta, A.; Nuytten, T.; Celano, U.; Sutar, S.; Pourtois, G.; Caymax, M.; Paredis, K.; Vandervorst, W.; Lin, D.; De Gendt, S.; Barla, K.; Huyghebaert, C.; Asselberghs, I.; Radu, I. Layer-Controlled Epitaxy of 2D Semiconductors: Bridging Nanoscale Phenomena to Wafer-Scale Uniformity. *Nanotechnology* **2018**, *29* (42), 425602.
(11) Hofmann, W. K. Thin Films of Molybdenum and Tungsten Disulphides by Metal Organic Chemical Vapour Deposition. *J. Mater. Sci.* **1988**, *23* (11), 3981−3986.
(12) Chung, J. W.; Dai, Z. R.; Ohuchi, F. S. WS2 Thin Films by Metal Organic Chemical Vapor Deposition. *J. Cryst. Growth* **1998**, *186* (1), 137−150.
(13) Choudhury, T. H.; Simchi, H.; Boichot, R.; Chubarov, M.; Mohney, S. E.; Redwing, J. M. Chalcogen Precursor Effect on Cold-Wall Gas-Source Chemical Vapor Deposition Growth of WS2. *Cryst. Growth Des.* **2018**, *18* (8), 4357−4364.
(14) Grundmann, A.; Andrzejewski, D.; Kümmell, T.; Bacher, G.; Heuken, M.; Kalisch, H.; Vescan, A. H2S-Free Metal-Organic Vapor Phase Epitaxy of Coalesced 2D WS2 Layers on Sapphire. *MRS Adv.* **2019**, *4* (10), 593−599.
(15) Dumcenco, D.; Ovchinnikov, D.; Marinov, K.; Lazić, P.; Gibertini, M.; Marzari, N.; Sanchez, O. L.; Kung, Y.-C.; Krasnozhon, D.; Chen, M.-W.; Bertolazzi, S.; Gillet, P.; Fontcuberta i Morral, A.; Radenovic, A.; Kis, A. Large-Area Epitaxial Monolayer MoS 2. *ACS Nano* **2015**, *9* (4), 4611−4620.
(16) Du, L.; Yu, H.; Xie, L.; Wu, S.; Wang, S.; Lu, X.; Liao, M.; Meng, J.; Zhao, J.; Zhang, J.; Zhu, J.; Chen, P.; Wang, G.; Yang, R.; Shi, D.; Zhang, G. The Effect of Twin Grain Boundary Tuned by Temperature on the Electrical Transport Properties of Monolayer MoS2. *Crystals* **2016**, *6* (9), 115.
(17) Pulkin, A.; Yazyev, O. V. Spin- and Valley-Polarized Transport across Line Defects in Monolayer MoS2. *Phys. Rev. B: Condens. Matter Mater. Phys.* **2016**, *93* (4), 41419.
(18) Yu, H.; Liao, M.; Zhao, W.; Liu, G.; Zhou, X. J.; Wei, Z.; Xu, X.; Liu, K.; Hu, Z.; Deng, K.; Zhou, S.; Shi, J. A.; Gu, L.; Shen, C.; Zhang, T.; Du, L.; Xie, L.; Zhu, J.; Chen, W.; Yang, R.; et al. Wafer-Scale Growth and Transfer of Highly-Oriented Monolayer MoS2 Continuous Films. *ACS Nano* **2017**, *11* (12), 12001−12007.
(19) Zhang, X.; Choudhury, T. H.; Chubarov, M.; Xiang, Y.; Jariwala, B.; Zhang, F.; Alem, N.; Wang, G.-C.; Robinson, J. A.; Redwing, J. M. Diffusion-Controlled Epitaxy of Large Area Coalesced WSe2Monolayers on Sapphire. *Nano Lett.* **2018**, *18* (2), 1049−1056.
(20) Chen, L.; Liu, B.; Ge, M.; Ma, Y.; Abbas, A. N.; Zhou, C. Step-Edge-Guided Nucleation and Growth of Aligned WSe2 on Sapphire *via* a Layer-over-Layer Growth Mode. *ACS Nano* **2015**, *9* (8), 8368−8375.
(21) Hwang, Y.; Shin, N. Hydrogen-Assisted Step-Edge Nucleation of MoSe2Monolayers on Sapphire Substrates. *Nanoscale* **2019**, *11* (16), 7701−7709.
(22) Rau, H.; Kutty, T. R. N.; de Carvalho, J. R. F. G. High Temperature Saturated Vapour Pressure of Sulphur and the Estimation of Its Critical Quantities. *J. Chem. Thermodyn.* **1973**, *5* (2), 291−302.
(23) M, T.; Late, D. J. Temperature Dependent Phonon Shifts in Single-Layer WS2. *ACS Appl. Mater. Interfaces* **2014**, *6* (2), 1158−1163.
(24) International Centre for Diffraction Data, Powder Diffraction File: 04-003-4478, 2017.
(25) Xiang, Y.; Sun, X.; Valdman, L.; Zhang, F.; Choudhury, T. H.; Chubarov, M.; Robinson, J. A.; Redwing, J.; Terrones, M.; Ma, Y.; Gao, L.; Washington, M. A.; Lu, T.-M.; Wang, G.-C. Monolayer MoS2 on Sapphire: An Azimuthal Reflection High-Energy Electron Diffraction Perspective. *2D Mater.* **2021**, *8*, 02503.
(26) Lin, Y. C.; Jariwala, B.; Bersch, B. M.; Xu, K.; Nie, Y.; Wang, B.; Eichfeld, S. M.; Zhang, X.; Choudhury, T. H.; Pan, Y.; Addou, R.; Smyth, C. M.; Li, J.; Zhang, K.; Haque, M. A.; Fölsch, S.; Feenstra, R. M.; Wallace, R. M.; Cho, K.; Fullerton-Shirey, S. K.; et al. Realizing Large-Scale, Electronic-Grade Two-Dimensional Semiconductors. *ACS Nano* **2018**, *12* (2), 965−975.
(27) Reifsnyder Hickey, D.; Nayir, N.; Chubarov, M.; Choudhury, T. H.; Bachu, S.; Miao, L.; Wang, Y.; Qian, C.; H. Crespi, V.; M. Redwing, J.; van Duin, A. C. T.; Alem, N. Illuminating Invisible Grain Boundaries in Coalesced Single-Orientation WS_2 Monolayer Films. 2020, arXiv:2006.11668 arXiv eprint archive. https://arxiv.org/abs/2006.11668
(28) van der Zande, A. M.; Huang, P. Y.; Chenet, D. A.; Berkelbach, T. C.; You, Y.; Lee, G.-H.; Heinz, T. F.; Reichman, D. R.; Muller, D. A.; Hone, J. C. Grains and Grain Boundaries in Highly Crystalline Monolayer Molybdenum Disulphide. *Nat. Mater.* **2013**, *12* (6), 554−561.
(29) Azizi, A.; Zou, X.; Ercius, P.; Zhang, Z.; Elías, A. L.; Perea-López, N.; Stone, G.; Terrones, M.; Yakobson, B. I.; Alem, N. Dislocation Motion and Grain Boundary Migration in Two-Dimensional Tungsten Disulphide. *Nat. Commun.* **2014**, *5* (1), 4867.
(30) Azizi, A.; Eichfeld, S.; Geschwind, G.; Zhang, K.; Jiang, B.; Mukherjee, D.; Hossain, L.; Piasecki, A. F.; Kabius, B.; Robinson, J. A.; Alem, N. Freestanding van der Waals Heterostructures of Graphene and Transition Metal Dichalcogenides. *ACS Nano* **2015**, *9* (5), 4882−4890.
(31) Ago, H.; Endo, H.; Solís-Fernández, P.; Takizawa, R.; Ohta, Y.; Fujita, Y.; Yamamoto, K.; Tsuji, M. Controlled van der Waals Epitaxy of Monolayer MoS2 Triangular Domains on Graphene. *ACS Appl. Mater. Interfaces* **2015**, *7* (9), 5265−5273.
(32) Dong, J.; Ding, F. The Epitaxy of 2D Materials Growth. *Nat. Commun.* **2020**, *11*, 5862.
(33) Reifsnyder Hickey, D.; Yilmaz, D. E.; Chubarov, M.; Bachu, S.; H Choudhury, T.; Miao, L.; Qian, C.; Redwing, J. M.; van Duin, A. C. T.; Alem, N. Formation of Metal Vacancy Arrays in Coalesced WS2 Monolayer Films. *2D Mater.* **2021**, *8* (1), 11003.
(34) Chen, W.; Zhao, J.; Zhang, J.; Gu, L.; Yang, Z.; Li, X.; Yu, H.; Zhu, X.; Yang, R.; Shi, D.; Lin, X.; Guo, J.; Bai, X.; Zhang, G. Oxygen-Assisted Chemical Vapor Deposition Growth of Large Single-Crystal and High-Quality Monolayer MoS2. *J. Am. Chem. Soc.* **2015**, *137* (50), 15632−15635.
(35) Tongay, S.; Suh, J.; Ataca, C.; Fan, W.; Luce, A.; Kang, J. S.; Liu, J.; Ko, C.; Raghunathanan, R.; Zhou, J.; Ogletree, F.; Li, J.; Grossman, J. C.; Wu, J. Defects Activated Photoluminescence in Two-Dimensional Semiconductors: Interplay between Bound, Charged, and Free Excitons. *Sci. Rep.* **2013**, *3*, 2657.
(36) Dobrovinskaya, E. R.; Lytvynov, L. A.; Pishchik, V. *Properties of Sapphire. In: Sapphire. Micro- and Opto-Electronic Materials, Structures, and Systems*; Springer: Boston, 2009.
(37) McCreary, A.; Berkdemir, A.; Wang, J.; Nguyen, M. A.; Elías, A. L.; Perea-López, N.; Fujisawa, K.; Kabius, B.; Carozo, V.; Cullen, D. A.; Mallouk, T. E.; Zhu, J.; Terrones, M. Distinct Photoluminescence and Raman Spectroscopy Signatures for Identifying Highly Crystalline WS2Monolayers Produced by Different Growth Methods. *J. Mater. Res.* **2016**, *31* (7), 931−944.
(38) Liu, Z.; Amani, M.; Najmaei, S.; Xu, Q.; Zou, X.; Zhou, W.; Yu, T.; Qiu, C.; Birdwell, A. G.; Crowne, F. J.; Vajtai, R.; Yakobson, B. I.; Xia, Z.; Dubey, M.; Ajayan, P. M.; Lou, J. Strain and Structure

https://dx.doi.org/10.1021/acsnano.0c06750
ACS Nano 2021, 15, 2532−2541

Heterogeneity in MoS2 Atomic Layers Grown by Chemical Vapour Deposition. *Nat. Commun.* **2014**, *5* (1), 5246.

(39) Plechinger, G.; Nagler, P.; Kraus, J.; Paradiso, N.; Strunk, C.; Schüller, C.; Korn, T. Identification of Excitons, Trions and Biexcitons in Single-Layer WS2. *Phys. Status Solidi RRL* **2015**, *9* (8), 457−461.

(40) Kim, M. S.; Yun, S. J.; Lee, Y.; Seo, C.; Han, G. H.; Kim, K. K.; Lee, Y. H.; Kim, J. Biexciton Emission From Edges and Grain Boundaries of Triangular WS2Monolayers. *ACS Nano* **2016**, *10* (2), 2399−2405.

(41) Sebastian, A.; Zhang, F.; Dodda, A.; May-Rawding, D.; Liu, H.; Zhang, T.; Terrones, M.; Das, S. Electrochemical Polishing of Two-Dimensional Materials. *ACS Nano* **2019**, *13* (1), 78−86.

(42) Schulman, D. S.; Sebastian, A.; Buzzell, D.; Huang, Y.-T.; Arnold, A. J.; Das, S. Facile Electrochemical Synthesis of 2D Monolayers for High-Performance Thin-Film Transistors. *ACS Appl. Mater. Interfaces* **2017**, *9* (51), 44617−44624.

(43) Yun, S. J.; Chae, S. H.; Kim, H.; Park, J. C.; Park, J.-H.; Han, G. H.; Lee, J. S.; Kim, S. M.; Oh, H. M.; Seok, J.; Jeong, M. S.; Kim, K. K.; Lee, Y. H. Synthesis of Centimeter-Scale Monolayer Tungsten Disulfide Film on Gold Foils. *ACS Nano* **2015**, *9* (5), 5510−5519.

(44) Xuan, Y.; Jain, A.; Zafar, S.; Lotfi, R.; Nayir, N.; Wang, Y.; Choudhury, T. H.; Wright, S.; Feraca, J.; Rosenbaum, L.; Redwing, J. M.; Crespi, V.; van Duin, A. C. T. Multi-Scale Modeling of Gas-Phase Reactions in Metal-Organic Chemical Vapor Deposition Growth of WSe2. *J. Cryst. Growth* **2019**, *527*, 125247.

(45) Chubarov, M.; Choudhury, T. H.; Zhang, X.; Redwing, J. M. In-Plane X-Ray Diffraction for Characterization of Monolayer and Few-Layer Transition Metal Dichalcogenide Films. *Nanotechnology* **2018**, *29* (5), 55706.

(46) Huang, P. Y.; Ruiz-Vargas, C. S.; van der Zande, A. M.; Whitney, W. S.; Levendorf, M. P.; Kevek, J. W.; Garg, S.; Alden, J. S.; Hustedt, C. J.; Zhu, Y.; Park, J.; McEuen, P. L.; Muller, D. A. Grains and Grain Boundaries in Single-Layer Graphene Atomic Patchwork Quilts. *Nature* **2011**, *469* (7330), 389−392.

https://dx.doi.org/10.1021/acsnano.0c06750
ACS Nano 2021, 15, 2532−2541